BIOELECTRICITY
Volume 00, Number 00, 2020

DOI: 10.1089/bioe.2020.0023

Thermochromic Tissue Phantoms for Evaluating Temperature Distribution in Simulated Clinical Applications of Pulsed Electric Field Therapies

Michael B. Sano, PhD[1] and Matthew R. DeWitt, PhD[2]

Abstract

Background: Irreversible electroporation (IRE) induces cell death through nonthermal mechanisms, however, in extreme cases, the treatments can induce deleterious thermal transients. This study utilizes a thermochromic tissue phantom to enable visualization of regions exposed to temperatures above 60°C.
Materials and Methods: Poly(vinyl alcohol) hydrogels supplemented with thermochromic ink were characterized and processed to match the electrical properties of liver tissue. Three thousand volt high-frequency IRE protocols were administered with delivery rates of 100 and 200 μs/s. The effect of supplemental internal applicator cooling was then characterized.
Results: Baseline treatments resulted thermal areas of 0.73 cm^2, which decreased to 0.05 cm^2 with electrode cooling. Increased delivery rates (200 μs/s) resulted in thermal areas of 1.5 and 0.6 cm^2 without and with cooling, respectively.
Conclusions: Thermochromic tissue phantoms enable rapid characterization of thermal effects associated with pulsed electric field treatments. Active cooling of applicators can significantly reduce the quantity of tissue exposed to deleterious temperatures.

Keywords: high-frequency irreversible electroporation, thermal injury, nonthermal ablation

Introduction

Irreversible electroporation (IRE) is an emerging cancer therapy[1–3] that uses pulsed electric fields (PEFs) to permanently disrupt cell membranes within a focal tissue volume. Clinically, two or more partially active electrode applicators are inserted into tissue to destroy nearby cells, while sparing the underlying extracellular matrix from thermal effects.[4] IRE is considered a nonthermal ablation modality due to the presumption that the lethal action of the PEF is not dependent on local tissue temperatures but rather results from a combination of reversible and permanent membrane destabilization leading to cell death.[5–9] Due to the theoretically nonthermal, membrane-targeting mechanism, IRE is typically applied clinically for particular cases that are contraindicated for surgery or thermal ablations, due to sensitive anatomical location (e.g. nearby vital structures).[10]

Current IRE treatments are administered clinically by a single FDA-approved device termed the NanoKnife (NK-IRE; AngioDynamics, Latham, NY). NK-IRE aims to create significant therapeutic volumes (>25 cm^3) where the local electric field is above $\sim$500 V/cm,[5,6,11,12] resulting in applied currents in the range of 25–50 A.[13–15] Application of such high currents has the potential to significantly raise local tissue temperatures due to Joule heating.[16,17] Currently, NK-IRE does not use active temperature sensing or a temperature feedback loop, and treatments that induce significant thermal injury can be inadvertently administered.[13,18,19] This is a substantial challenge as NK-IRE is generally used clinically to treat tumors where permanent thermal damage must be avoided.[20]

To address this challenge and minimize the risk for thermal damage, several approaches have been proposed. The simplest approach is to minimize electrode exposures to decrease current delivery or decrease the energy delivery rate (pulse repetition rate)[19] to minimize average power dissipation. However, these techniques can significantly increase treatment times and reduce treatment volumes. Alternative passive strategies have been investigated, which use phase change,[21] irrigated,[22] or internally cooled electrodes,[23] to minimize transient temperature rises, however, none of these techniques are currently used in clinical settings.

[1]UNC/NCSU Joint Department of Biomedical Engineering, Raleigh, North Carolina, USA.
[2]Luna Innovations, Inc., Charlottesville, Virginia, USA.

Ideally, NK-IRE and other PEF applications[24–27] minimize the potential for thermal damage and would be uniformly evaluated *in vivo* within the same target organ to account for the dynamic electrical and thermal responses associated with treatments occurring in perfused tissue.[28] However, ethical and economic constraints often necessitate the use of alternative models for early-stage evaluation. These PEF therapies should be evaluated in a model that replicates the electrical and thermal properties of *in vivo* tissue as well as the geometric size so that instruments intended for clinical use can be evaluated without modification. Historically, *ex vivo* bovine liver has served this role,[29–33] and recent developments in organ preservation[34] have enabled the use of viable *ex vivo* liver tissue for evaluating PEF therapies.[11,23,35] However, precise computational quantification of thermal injury in these models can be challenging due to limited contrast between the injured and normal tissue or the need for expensive thermometry methods (e.g. magnetic resonance thermometry).

Tissue-mimicking phantoms are beginning to see use for evaluating novel therapeutics[36] and could be used to evaluate the thermal profile of ablative therapies such as IRE. These phantoms can include cells and microfluidic channels[37] to evaluate the cellular effects of therapies,[38] determine lethal thresholds,[39,40] and can be used to evaluate energy depositions before clinical use, ensuring safety profiles while overcoming the limitations of traditional *ex vivo* models describe above. Thermochromism is the property of a substance that can change colors due to a change in temperature and thermochromic materials have been utilized in product labeling, thermometers, novelty items, and recently in tissue-mimicking phantoms for thermal ablation therapies.[36,41,42]

Here we modified a validated thermochromic tissue phantom concept,[36,41] previously utilized to visualize radiofrequency ablation (RFA) thermal dynamics, to evaluate deleterious thermal effects associated with specific PEF treatments such as NK-IRE. This phantom was calibrated to exhibit the electrical properties of liver tissue. The model was tuned to rapidly transition in color between 55°C and 60°C, as these temperatures are associated with the induction of instantaneous thermal injury[43] and should be avoided in IRE treatments, especially near critical structures. After validation, the tissue model was used to evaluate techniques for reducing thermal injury in PEF treatments: (1) manually reducing delivery rates and (2) actively internally cooling the applicator. We then utilize the calibrated phantom to demonstrate that active cooling of the electrode applicator can reduce the extent of thermal injury by 93%. Active cooling enabled treatments that were delivered at twice the rate (200 μs/s) and required half of the duration (100 s) of baseline treatments, reducing the volume of tissue exposed to temperatures above 60°C compared with controls.

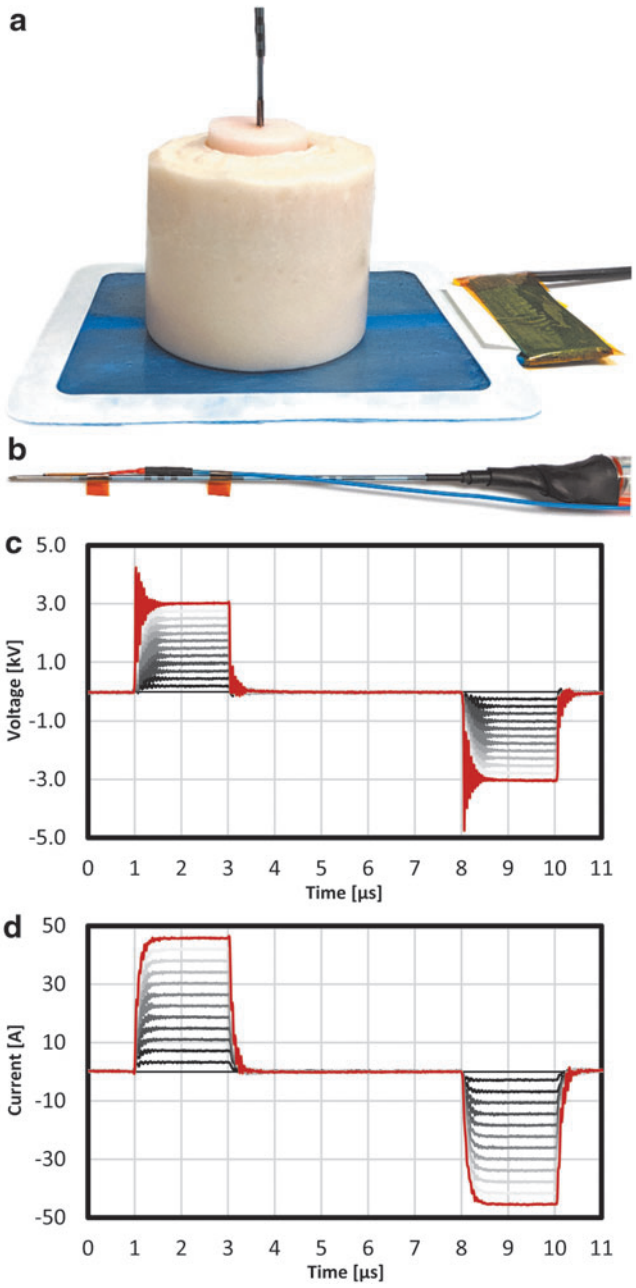

FIG. 1. The experimental thermochromic tissue phantom consisted of **(a)** a base used to make contact with the grounding pad and a replaceable sample into which the **(b)** single-electrode applicator was inserted. A fiberoptic temperature sensor adjacent to the electrode was used to measure temperature throughout the treatments. **(c)** Voltage and **(d)** current waveforms were recorded for the ramp up procedure (shown) and throughout the treatment.

Materials and Methods

Tissue phantom material

The tissue phantom material utilized in this study (Fig. 1) is based on poly(vinyl alcohol) (PVA) hydrogels that have previously been developed to mimic the mechanical properties of human livers[44] and were modified to mimic the electric properties relevant to IRE therapies. The phantom material critically utilizes a commercially available thermochromic ink (TCR Hallcrest, Inc., Glenview, IL), which permanently changes color from white to magenta around 60°C, allowing the phantom material to report on the temperature distribution around the clinical applicators.

Aqueous stock solutions of 12% w/v PVA (130,000 M_w) were first prepared by dissolving PVA (99% hydrolyzed, 563900-500G; Sigma Aldrich, St. Louis, MO) in deionized water for 3 h at 80°C using magnetic stirring. The phantom formulation, shown in Table 1, was prepared for PEF studies by adjusting salinity to match the electrical properties of

Table 1. Thermochromic Phantom Formulation

Component	*Proportion (%)*
Deionized water	95 (v/v)
99% hydrolyzed PVA ($M_w = 130{,}000$)	12 (w/v)
Magenta MB60°C concentrate	5 (v/v)
NaCl	0.9 (w/v)

NaCl, sodium chloride; PVA, poly(vinyl alcohol).

biological tissues and was based on previous literature.[36] Briefly, after the PVA-water solution was thoroughly mixed, the stock solutions were allowed to return to room temperature to avoid temperature effects when mixed with the thermochromic ink. Ninety-five milliliters of PVA solution was then mixed with 5 mL of MB Magenta NH 60°C concentrate (5% v/v) (LCR Hallcrest, LLC, Glenview) and sodium chloride (NaCl) was added (0.9% w/v) to impart electrical conductivity. The final solution was stirred manually and was immediately transferred to cylindrical molds and sealed. The solutions then underwent two 24-h freeze/thaw (24 h at −20°C, 12 h at room temperature) cycles to form the PVA-hydrogel structure, following freeze/thaw methods previous described in literature.[45]

A two-component tissue phantom was created to enable the evaluation of multiple samples within the same experimental setup (Fig. 1a). A 59-mm-diameter, 490-mm-tall phantom body, or base, was created by pouring uncrosslinked material into a flat-bottomed sample cup. A 30-mm-wide, 36-mm-deep sample chamber, or void, was then created by securing a 50 mL Falcon tube in the center of the sample cup. The assembly was then frozen overnight to crosslink the material. Once solidified, the phantom body was stored in deionized (DI) water (4 days) before use to normalize conductivity. Experimental samples, or plugs, were similarly created by aliquoting base material into 50 mL Falcon tubes, freezing overnight, followed by storage in DI water.

Characterization of electrical response

To characterize the electrical properties of the phantom material, 25-mm-diameter, 5–12-mm-thick cylindrical samples were created. The impedance of the samples was then measured using a Bode 100 (Omicron Electronics, Inc., Houston, TX) impedance analyzer by placing the samples between two rectangular stainless steel electrodes and evaluating the system impedance at 10 kHz, 100 kHz, and 1 MHz, representing the characteristic frequencies associated with electrical pulses between 1 and 100 μs in duration. The electrical conductivity (σ) of the samples was then calculated as follows:

$$\sigma = \frac{L}{Z \cdot A} \tag{1}$$

where A was the surface area of the sample, L was the material thickness, and Z was the impedance. These values were then averaged and are presented as mean ± standard deviation. To evaluate if storage conditions can impact the electrical characteristics of these phantoms, a subset of samples were stored in deionized water for 1 h and 4 days (Fig. 2) before measurement.

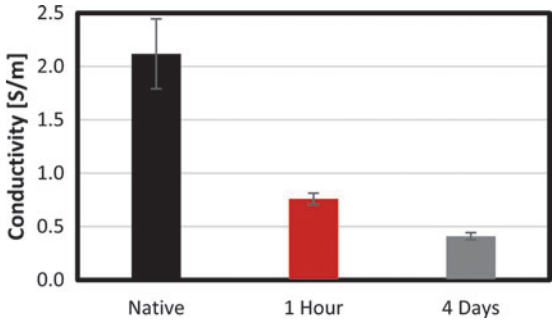

FIG. 2. Measured conductivity of poly(vinyl alcohol)-thermochromic hydrogel tissue phantom after 1 h or 4 days of soaking in deionized water.

Characterization of thermal response

To characterize the thermochromic response of the phantoms, the material was sectioned into cubes measuring ~1 cm on each edge. A 1 L water bath with mild stirring was heated to 30°C, 35°C, 40°C, 45°C, 50°C, 55°C, or 60°C using a standard plate heater (H3760-HS; Benchmark Scientific, Sayreville, NJ) and a fiberoptic temperature sensor (FOTEMP; Micronor, Inc., Camarillo, CA). When a stable temperature was achieved, the cubes were then placed directly in the circulating water for a duration of 400 s, twice the duration of the longest experimental treatment examined in this study, such that any thermochromic transitions approached steady state.

To characterize the time-dependent thermal response, 1 cm cubes were placed in a 60°C water bath for 25, 50, 100, 200, and 400 s. Following the specified heat treatment, all samples were removed from the water bath and quenched in room temperature deionized water. Characterization of the material at temperatures above 60°C was attempted using this method; however, these treatments resulted in complete disintegration of the material.

All samples were imaged in a light box with consistent angle, distance, and lighting. The images were then white balanced via a white object in all photographs using Adobe Photoshop (2017.0.1; Adobe, Inc., San Jose, CA) and were imported into ImageJ (1.51j8; NIH), where they were converted into 8-bit grayscale images. The 1 cm cubes used to characterize the thermal response were evaluated by calculating the mean grayscale value (0–255) of a square region measuring 0.75 × 0.75 cm. Three different photographs with each cube rotated to a different geometric face were evaluated ($n = 12$, 4 cubes, 3 faces) yielding 12 measurements for each temperature set point. The values were then averaged and are reported as mean ± standard deviation.

Energy delivery

PEF treatments were administered via an applicator and grounding pad approach (A+GP). This approach produces spherical ablation zones surrounding the exposed electrode[46,47] and simplifies both the surgical approach[48] and computational treatment evaluation.[49,50] A 1.44-mm-diameter internally cooled clinical RFA applicator (Cool-Tip RF ACT1520; Medtronic, Inc., Minneapolis, MN) with a 2 cm exposed electrode was modified to enable high-voltage pulse delivery. This was accomplished by removing the applicator handle and replacing the single low-voltage electrical lead

with 10 kV rated silicone-coated wire (6733-2; Pomona Electronics, Inc., Everett, WA). Polyimide tape was wrapped around any exposed metal on the proximal end of the applicator and the assembly was covered in heat shrink tubing (Fig. 1b). A 200-μm-diameter fiberoptic temperature sensor (TS5; Micronor, Inc.) was affixed to the distal end of the applicator such that the sensing region was approximately half way along the electrode surface (8.6 mm from the insulation and 10.6 mm from the electrode tip). A strip of polyimide tape was adhered to the applicator body 5 mm above the insulation/electrode interface to enable consistent placement of the electrode below the phantom surface.

An electrical return path was established by placing the tissue phantom assembly on an adhesive grounding pad (E7507; Covidien, Inc., Dublin, Ireland). This was similarly modified to replace the original low-voltage rated cable with 10 kV rated silicone-coated wire. Treatments were administered via a custom-built pulse generation system based on an H-Bridge topology, which recorded voltage, current, and temperature in real time. As traditional NK-IRE waveforms have been shown to produce intense electrical arcing with the A+GP approach,[47,50] an alternative continuous high-frequency IRE (H-FIRE) protocol was evaluated. Each treatment consisted of a bipolar waveform with a 2 μs positive phase, a 5 μs delay, and a 2 μs negative phase (Fig. 1c, d). This waveform was repeated at either 25 or 50 Hz to achieve energy delivery rates of 100 or 200 μs/s, respectively. These waveforms were delivered continuously until a total integrated energized time (IET) of 0.02 s was achieved (5000 × waveforms containing 10,000 × pulses). This electrical dose was chosen to replicate values typically used in NK-IRE and H-FIRE protocols. Similarly a baseline delivery rate of 100 μs/s was chosen to match NK-IRE treatments that typically deliver a single 50–100 μs pulse with cardiac synchronization (~ 1 Hz, 50–100 μs/s). All treatments were administered with a voltage of 3000 V to match the maximum voltage utilized clinically with NK-IRE.

A subset of experiments were conducted with internal electrode cooling. This was accomplished by perfusing the applicator at a rate of 2 mL/min with ice water via a peristaltic pump (EW-77921-65; Cole-Palmer, Vernon Hills, IL) attached to the applicators fluid inlet tubing. Following treatment, the tissue phantoms were subjected to two overnight freeze/thaw cycles to solidify any material that had melted during the treatment and to match the processing associated with the characterization process.

Quantification of treatment zones

The thermal injury area created by the PEF treatments was calculated by white balancing and converting all photographs into 8-bit grayscale images. These images were then thresholded to values of 191–255 using the IsoData algorithm (Fig. 3), corresponding to the pixel intensity found for exposures of 60°C for 400 s. The area above the threshold value was then calculated for a region measuring 2.0 × 2.5 cm within each treatment sample ($n = 6$, 3 replicates, 2 faces), yielding six measurements for each treatment. The values were then averaged and are reported as mean ± standard deviation.

Statistical analysis was conducted via one-way Student's *t*-tests with an alpha level of 0.05 indicating significance using JMP (V14.1.0; SAS Institute, Inc., Cary, NC)

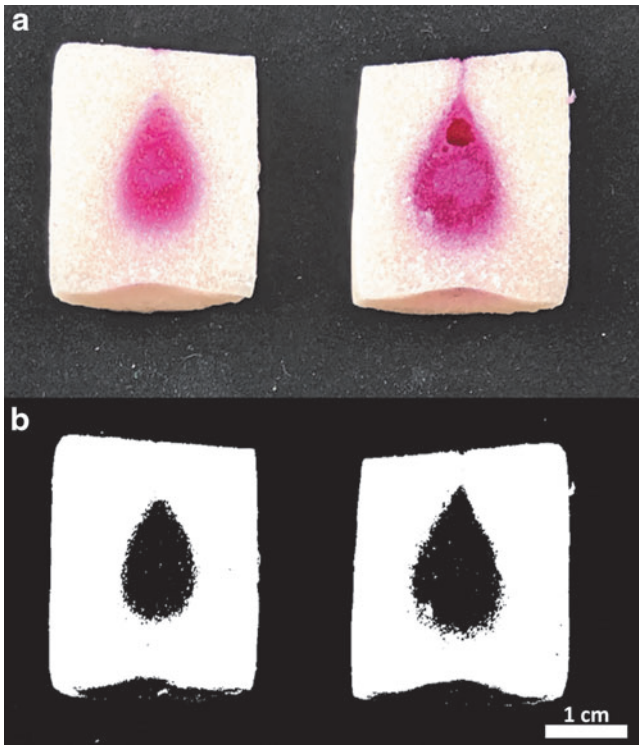

FIG. 3. Photochromic phantom following a 0.02-s IET treatment with an energy delivery rate of 200 μs/s **(a)** before and **(b)** after image processing to identify tissue exposed to 60°C or greater temperatures. IET, integrated energized time.

Results

Characterization of phantom electrical conductivity

There was not a statistically significant difference in conductivity values between data acquired at 10 kHz, 100 kHz, or 1 MHz ($p > 0.73$). The native phantom material had a mean electrical conductivity of 2.12 ± 0.33 S/m averaged across all frequency values. This decreased to 0.76 ± 0.05 and 0.41 ± 0.03 S/m after 1 h and 4 days storage in DI water, respectively. As liver conductivity has previously been reported in this range,[51] all further experiments utilized 4 days of DI water storage before use (Fig. 2).

Characterization of phantom thermal response

To characterize the time-domain response of the phantoms, 1 cm^3 samples were placed in 60°C water for up to 400 s (Fig. 4a). These samples had a baseline pixel intensity of 249 ± 5 (Fig. 4b). After 25 s of exposure, the pixel intensity was 248 ± 5, which was not significantly less than baseline ($p = 0.61$). The pixel intensity dropped significantly ($p < 0.0001$) between 50 (240 ± 7) and 100 s (201 ± 6) after which it appeared to reach a steady state. However, statistically significant decreases in pixel intensity did occur between the 100-, 200 (195 ± 7, $p = 0.005$)-, and 400-s (191 ± 6, $p = 0.0049$) exposure samples (Fig. 4b). To characterize the temperature-domain response of the phantoms, 1 cm^3 samples were placed in 30–60°C water for 400 s (Fig. 4c). Statistically significant differences were found between the 50°C (240 ± 5)

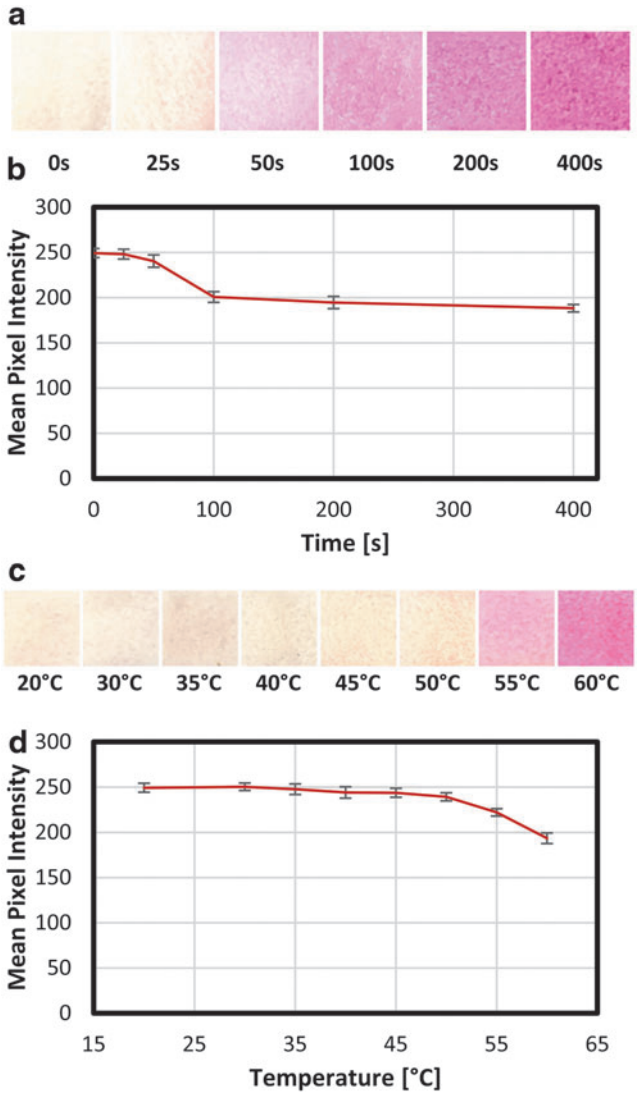

FIG. 4. The photochromic phantoms exhibited a time-dependent and temperature-dependent response. **(a)** Time dependent response of the phantoms following a 60°C exposure. **(b)** Mean grayscale pixel intensity versus exposure time. **(c)** Temperature-dependent response following 400-s exposures to temperatures between 30°C and 60°C. **(d)** Mean grayscale pixel intensity versus exposure temperature. Baseline data (20°C) were acquired from samples that remained at room temperature.

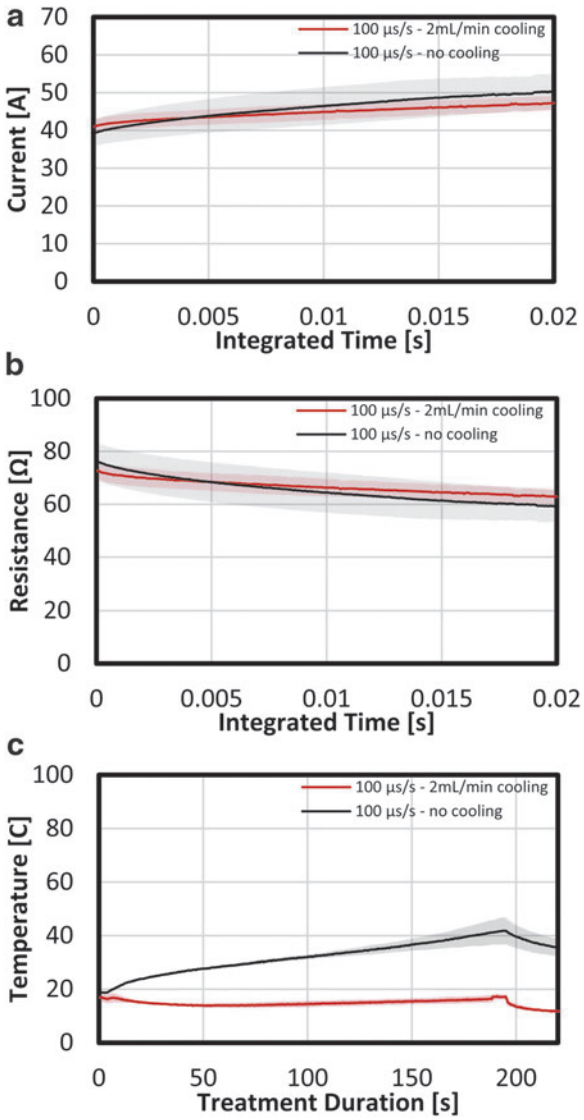

FIG. 5. Comparison of transient **(a)** current, **(b)** resistance, and **(c)** temperature profiles during cooled and non-cooled 3000 V, 002-s IET treatments administered at a rate of 100 μs/s.

and 55°C (222 ± 4, $p < 0.0001$), as well as the 55°C and 60°C (191 ± 6, $p < 0.001$) samples, but not between any other adjacent temperature pairs ($p > 0.54$) (Fig. 4d).

Electrical and thermal response during PEF treatment

The initial resistance of the tissue phantom was measured to be 72.8 ± 4.4 Ω as averaged across all treatment groups. This corresponds to an initial treatment current of 41.0 ± 2.2 A. Similarly, all treatments were conducted at room temperature with initial measurements of $17.9°C \pm 1.2°C$ across all experiments. In the baseline treatment (100 μs/s, 0.02 s IET, no cooling), the mean treatment current increased from 39.2 to 50.3 A (Fig. 5a) corresponding to a resistance change from 76.4 to 59.1 Ω (Fig. 5b). During the 200-s baseline treatment, the mean temperature increased from 18.7°C to 41.8°C (Fig. 5c).

Actively cooling the applicator while delivering the baseline treatment (100 μs/s, 0.02 s IET, 2 mL/min) resulted in a less substantial current rise (40.9 to 47.2 A) than treatments without cooling (6.3 vs. 11.1 A increase). Similarly, a smaller resistance change (72.7 to 62.3 Ω) was observed for these treatments when the applicator was cooled. The use of ice water as the coolant resulted in a mean decrease in measured temperature over the 200-s treatment (Fig. 5c), with a final temperature of 17.1°C.

Similar current rises (Fig. 6a) and decreases in resistance (Fig. 6b) were observed when the energy delivery rate was increased to 200 μs/s. Without cooling, these treatments rapidly exceeded 65°C (Fig. 6c), resulting in a phase change in the phantom material. Actively cooling the probe during these treatments resulted in a muted temperature rise with a mean peak temperature of $24.4°C \pm 0.4°C$.

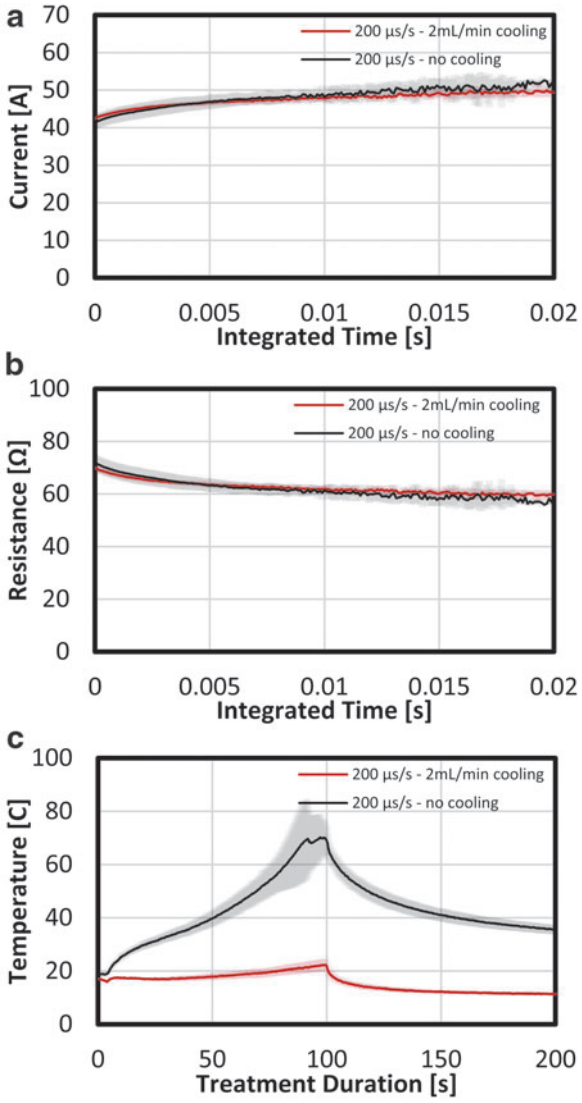

FIG. 6. Comparison of transient **(a)** current, **(b)** resistance, and **(c)** temperature profiles during cooled and noncooled 3000 V, 002-s IET treatments administered at a rate of 200 μs/s.

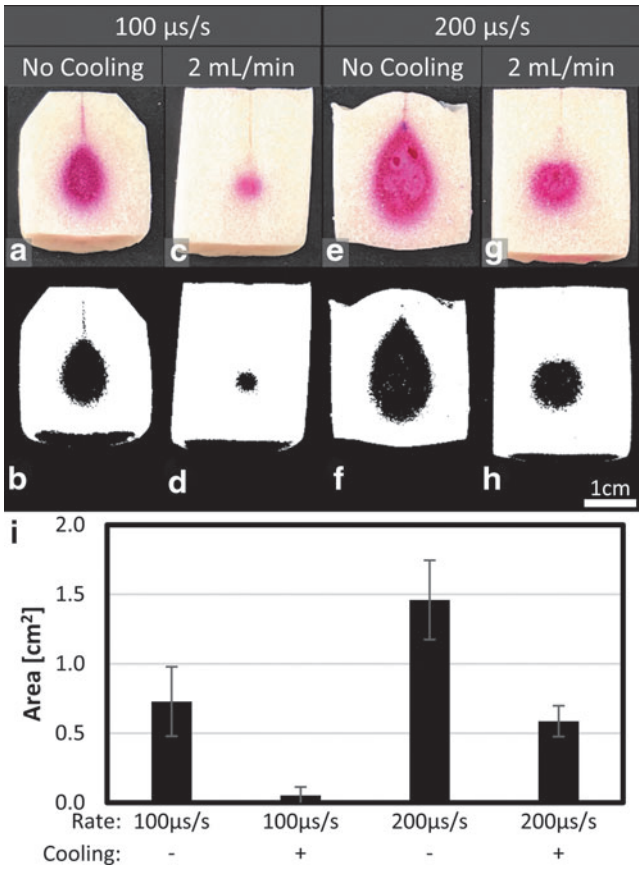

FIG. 7. Active cooling significantly reduces the quantity of phantom exposed to temperatures above 60°C in pulsed electric field treatments. Original images **(a, c, e, g)** were processed **(b, d, f, h)** to enable computational quantification of **(i)** tissue area exposed to temperatures of 60°C or greater. All consisted of 3000 V waveforms with a total dose of 0.02-s IET. Baseline treatments were administered with an energy delivery rate of **(a, b)** 100 μs/s without cooling and with **(c, d)** 2 mL/min of cooling. Treatments with the same dose delivered at a higher energy delivery rate of 200 μs/s **(e, f)** without and **(g, h)** with 2 mL/min of cooling.

Visualization of thermal injury zones

All treatments resulted in a visible color change within the phantom (Fig. 7a–h). Baseline treatments (100 μs/s, 0.02 s IET) resulted in a teardrop-shaped thermal zone with the narrowest region corresponding to the proximal end of the applicator approximately half-way down the length of the electrode (Fig. 7a, b). This thermal zone had a mean area of 0.73 ± 0.25 cm^2 (Fig. 7i). Active cooling of the applicator resulted in a significantly smaller ($p < 0.0001$) spherical thermal zone corresponding to approximately the distal tip of the electrode (Fig. 7c, d). Increasing the energy delivery rate to 200 μs/s (0.02 s IET) resulted in a teardrop-shaped thermal zone, which was significantly larger than ($p < 0.0001$) all other treatment groups (Fig. 7e, f), measuring 1.5 ± 0.3 cm^2. Active cooling of the applicator during this protocol (200 μs/s 0.02 s IET) resulted in a spherical thermal zone centered on the electrode tip, which measured 0.6 ± 0.1 cm^2. This was significantly smaller than the corresponding noncooled treatment ($p < 0.0001$), but was not significantly smaller than the noncooled baseline treatment ($p = 0.224$).

Discussion

While many PEF therapies, including NK-IRE, are considered to be nonthermal[6,7,9,52–54] due to their induction of cell death via mechanisms that are not dependent on local tissue temperatures,[55,56] these treatments have the potential to induce deleterious thermal transients[18] that could result in thermal injury to adjacent tissues.[19] Local tissue temperatures are generally not measured or accounted for in clinical treatments and rare examples of coagulative necrosis,[18] abscesses,[57] fistulas,[58] and thrombosis[59] may be due, in part, to unintended thermal injury.

The tissue phantom model presented here may be a useful tool as part of clinical training or research and development for PEF treatments as it offers rapid feedback and near real-time visualization of treatments which induce temperatures

associated with thermal injury. This could be especially useful for evaluating treatments using elevated voltages (3000–10,000 V),[47] alternative pulse timing strategies,[39] applicator arrays,[60] or in novel delivery approaches.[61] In addition, the model has been tuned to exhibit the physical properties of liver tissue.[44] Formulations can be tuned to match needle-tissue forces for other tissues where PEFs can be delivered, such as kidneys.[62] The phantom recapitulated basic electrical characteristics of clinically relevant tissues with a final electrical conductivity of 0.41 S/m. This was approximately equivalent to the conductivity of healthy hepatic tissue and hepatic tumors (0.15–0.55 S/m).[51] However, these tissues tend to increase in conductivity over the measured range (10 kHz–1 MHz), a frequency-dependent response was not observed in this phantom material. The electrical properties of the tissue phantom introduced in this article were tuned using NaCl concentration and further by varying postfabrication soaking (Fig. 2). While tuned for liver tissue, the model could be further refined to match the tissue-specific electrical properties of various tissues through these parameters and the addition of nanomaterials such as carbon microcoils could be used to better recreate the frequency-dependent conductivity at higher frequencies if needed.[63]

The model was fabricated as a two-part phantom, with a reusable large base and smaller plug inserted into a center base-void to allow plug removal for rapid evaluation of temperature fields in the volumes nearest to the applicator and continued use of the larger base. Use of this two-part system can help reduce costs of the phantom and studies, and the plug diameter can be modified based on predicted ablation size. The tissue in the simulated ablation zone was modeled as a homogeneous volume without blood vessels or connective tissue, which may have distorted the electric field and altered the resulting ablation and thermal fields. While H-FIRE is hypothesized to be less susceptible to distortion by these anatomical structures,[64] it remains unclear if they can be ignored for treatment planning purposes and studying maximum temperature levels during NK-IRE and H-FIRE treatments. While simplified models can be sufficient for evaluating maximum temperatures, more complicated models, including the use of perfused vessels, might be necessary when accurate predictions of the local temperature distribution are required.

The extent or probability of inducing thermal injury typically depends on a combination of the maximum temperature and duration of exposure.[10] A single, universally accepted cumulative thermal dose parameter is not currently well defined and there is ongoing discussion of the most appropriate thermal dose parameter for estimating thermal damage as a function of time and temperature.[65,66] Thermal damage of human tissue at mild hyperthermic temperatures (43–45°C) typically requires exposure durations on the order of an hour to induce cell death or tissue injury.[43] One approach to describe thermal damage is to calculate the cumulative equivalent minutes at 43°C (CEM43°C).[67,68] According to this thermal dosage method, 2–3 s at 57°C resulted in similar survival of multiple cell lines as 270 min at 43°C, indicating that cells are sensitive to instantaneous temperature exposures from 55°C to 60°C.[69] As NK-IRE and PEF treatments typically aim to deliver the intended dose over 1–5 min and given that peak temperatures typically occur late in the treatment (30+ s), a 60°C threshold for the phantom is the most relevant criteria for studying NK-IRE. However, it may be feasible to combine multiple thermochromic dyes to achieve additional delineated temperature zones in therapies where other critical temperatures are relevant.

The overall resistance of the phantom decreased during each treatment (Figs. 5 and 6), potentially due to increased ionic conductivity as a function of temperature. This seems to indicate that a positive correlation between temperature and electrical conductivity, as seen in tissue,[28] exists. However, all of the treatments resulted in similar changes in impedance independent of the instantaneous temperature measurements. This indicates that treatment current and current change may not be ideal proxies for temperature measurement nor ideal metrics for predicting the extent of thermal injury.

Each of the experimental protocols investigated here resulted in localized color change within the phantom despite some having recorded temperatures below 45°C. This was likely due to the fiberoptic temperature sensor being placed at the electrode midpoint rather than the distal tip where the electric field, and thus Joule heating, would be at a maximum. This highlights the utility of tissue phantom models, which can illustrate spatial distribution of temperatures that can occur as a result of PEF treatments better than single-point-based temperature sensors. Similarly, color changes were observed in treatments administered within a 100-s window (Figs. 6 and 7e–g), indicating the ability of the phantom model to account for relatively short thermal transients, especially when these transients are greater than 60°C where thermal injury would be approximately instantaneous.

Active cooling of the applicators significantly reduced the volume of material exposed to 60°C or greater versus matched noncooled treatments (Fig. 7). With active cooling, regions of elevated temperature occurred near the distal tip of the electrode. This may be due to the internal fluid channel not extending all the way to the distal end of the electrode resulting in less efficient cooling at the tip. This region also likely corresponds to the region of highest electric field, and thus greatest extent of Joule heating, due to the sharp point at the end of the electrode.

This study has some important limitations. A single waveform, electrode configuration, and voltage were examined and modifications to these may affect the electric field distribution and thermal response observed in this model. All experiments were conducted at room temperature and equivalent treatments conducted *in vivo* or at physiological temperatures may result in larger volumes of tissue exposed to temperatures of 60°C or greater. The treatments administered here resulted in relatively high currents (39–53 A) and strategies designed to modify this parameter may affect the temperature distribution. The phantom model described is unable to provide cumulative temperature profiles and can only elucidate maximum temperatures. Additional computational modeling[50] or thermal imaging would be necessary to better understand spatially varying transient thermal profiles. In addition, while the model can be utilized to elucidate thermal profiles, it cannot detect the efficacy of the nonthermal IRE as it lacks incorporated living cells. Recent reports utilizing collagen-based, cell-containing hydrogels[39,70,71] demonstrate these additional models, which can be coupled with the thermochromic models for full investigation of efficacy and safety. Finally, the phantom material utilized here is not actively perfused and heat

transport characteristics may be different than those observed *in vivo*. The results presented here should not be utilized for clinical treatment planning unless validated in an *in vivo* model.

Conclusion

This study presented a modified thermochromic tissue phantom that can be utilized to visualize zones exposed to deleterious temperatures during PEF therapies. Internal active cooling of the applicators utilized significantly reduced the volume of material exposed to temperatures above 60°C, indicating that these strategies may be effective at mitigating the risk of thermal injury in *in vivo* clinical applications.

Authorship Confirmation Statement

M.R.D. developed and implemented modified protocols for creating the tissue phantoms, generated experimental data, assisted in the analysis, and wrote the article. M.B.S. generated experimental data, processed and analyzed the data, and wrote the article.

Author Disclosure Statement

M.B.S. and M.R.D. have pending and issued patents related to the article. M.B.S. receives royalties from AngioDynamics, Inc.

Funding Information

This work was supported, in part, by the UNC/NCSU Joint Department of Biomedical Engineering through their provisioning of start-up funding. Additional support was provided by the NCSU Chancellor's Innovation Fund.

References

1. Al-Sakere B, Andre F, Bernat C, et al. Tumor ablation with irreversible electroporation. PLoS One 2007;2:e1135. DOI: 10.1371/journal.pone.0001135
2. Edd JF, Horowitz L, Davalos RV, et al. In vivo results of a new focal tissue ablation technique: Irreversible electroporation. IEEE Trans Biomed Eng 2006;53:1409–1415. DOI: 10.1109/tmbe.2006.873745
3. Aycock KN, Davalos RV. Irreversible electroporation: Background, theory, and review of recent developments in clinical oncology. Bioelectricity 2019;1:214–234.
4. Davalos RV, Mir LM, Rubinsky B. Tissue ablation with irreversible electroporation. Ann Biomed Eng 2005;33:223–231. DOI: 10.1007/s10439-005-8981-8
5. Garcia PA, Pancotto T, Rossmeisl JH, Jr., et al. Nonthermal irreversible electroporation (N-TIRE) and adjuvant fractionated radiotherapeutic multimodal therapy for intracranial malignant glioma in a canine patient. Technol Cancer Res Treat 2011;10:73–83.
6. Garcia P, Rossmeisl JJ, Neal R, et al. Intracranial nonthermal irreversible electroporation: In vivo analysis. J Membr Biol 2010;236:127–136.
7. Ellis TL, Garcia PA, Rossmeisl JH, Jr., et al. Nonthermal irreversible electroporation for intracranial surgical applications: Laboratory investigation. J Neurosurg 2011;114:681–688.
8. Golberg A, Yarmush ML. Nonthermal irreversible electroporation: Fundamentals, applications, and challenges. IEEE Trans Biomed Eng 2013;60:707–714. DOI: 10.1109/TBME.2013.2238672
9. Garcia PA, Rossmeisl JH, Jr., Ellis TL, et al. Nonthermal irreversible electroporation as a focal ablation treatment for brain cancer. In: Hayat M, ed. Tumors of the Central Nervous System, vol 12. Dordrecht: Springer, 2014;171–182.
10. Agnass P, van Veldhuisen E, van Gemert MJ, et al. Mathematical modeling of the thermal effects of irreversible electroporation for in vitro, in vivo, and clinical use: A systematic review. Int J Hyperthermia 2020;37:486–505.
11. Sano MB, Neal RE, II, Garcia PA, et al. Towards the creation of decellularized organ constructs using irreversible electroporation and active mechanical perfusion. Biomed Eng Online 2010;9:83. DOI: 10.1186/1475-925X-9-83
12. Miklavcic D, Semrov D, Mekid H, et al. A validated model of in vivo electric field distribution in tissues for electrochemotherapy and for DNA electrotransfer for gene therapy. Biochim Biophys Acta 2000;1523:73–83.
13. van Gemert MJ, Wagstaff PG, de Bruin DM, et al. Irreversible electroporation: Just another form of thermal therapy? Prostate 2015;75:332–335.
14. Dunki-Jacobs EM, Philips P, Martin RC. Evaluation of resistance as a measure of successful tumor ablation during irreversible electroporation of the pancreas. J Am Coll Surg 2014;218:179–187.
15. Cornelis FH, Cindrič H, Kos B, et al. Peri-tumoral metallic implants reduce the efficacy of irreversible electroporation for the ablation of colorectal liver metastases. Cardiovasc Intervent Radiol 2020;43:84–93.
16. Shafiee H, Garcia PA, Davalos RV. A preliminary study to delineate irreversible electroporation from thermal damage using the arrhenius equation. J Biomech Eng 2009;131:074509.
17. Garcia PA, Rossmeisl JH, Jr., Neal RE, II, et al. A parametric study delineating irreversible electroporation from thermal damage based on a minimally invasive intracranial procedure. Biomed Eng Online 2011;10:34. DOI: 10.1186/1475-925x-10-34
18. Faroja M, Ahmed M, Appelbaum L, et al. Irreversible electroporation ablation: Is all the damage nonthermal? Radiology 2013;266:462–470.
19. Dunki-Jacobs E, Philips P, Martin I. Evaluation of thermal injury to liver, pancreas and kidney during irreversible electroporation in an in vivo experimental model. Br J Surg 2014;101:1113–1121.
20. Kurata K, Nomura S, Takamatsu H. Three-dimensional analysis of irreversible electroporation: Estimation of thermal and non-thermal damage. Int J Heat Mass Transf 2014;72:66–74.
21. Arena CB, Mahajan RL, Nichole Rylander M, et al. An experimental and numerical investigation of phase change electrodes for therapeutic irreversible electroporation. J Biomech Eng 2013;135:111009.
22. Wandel A, Ben-David E, Ulusoy BS, et al. Optimizing irreversible electroporation ablation with a bipolar electrode. J Vasc Interv Radiol 2016;27:1441–1450.e1442. DOI: 10.1016/j.jvir.2016.06.001.
23. O'Brien TJ, Bonakdar M, Bhonsle S, et al. Effects of internal electrode cooling on irreversible electroporation using a perfused organ model. Int J Hyperther 2018;35:44–55. DOI: 10.1080/02656736.2018.1473893
24. Nuccitelli R, Tran K, Sheikh S, et al. Optimized nanosecond pulsed electric field therapy can cause murine malignant melanomas to self-destruct with a single treatment. Int J Cancer 2010;127:1727–1736. DOI: 10.1002/ijc.25364

25. Schoenbach KH, Beebe SJ, Buescher ES. Intracellular effect of ultrashort electrical pulses. Bioelectromagnetics 2001;22:440–448.
26. Kos S, Tesic N, Kamensek U, et al. Improved specificity of gene electrotransfer to skin using pDNA under the control of collagen tissue-specific promoter. J Membr Biol 2015; 248:919–928.
27. Sersa G, Teissie J, Cemazar M, et al. Electrochemotherapy of tumors as in situ vaccination boosted by immunogene electrotransfer. Cancer Immunol Immunother 2015;64: 1315–1327.
28. Rossmann C, Haemmerich D. Review of temperature dependence of thermal properties, dielectric properties, and perfusion of biological tissues at hyperthermic and ablation temperatures. Crit Rev Biomed Eng 2014;42: 467–492.
29. Pfannenstiel A, Sebek J, Fallahi H, et al. Directional microwave ablation: Experimental evaluation of a 2.45-GHz applicator in ex vivo and in vivo liver. J Vasc Interv Radiol 2020;31:1170–1177.e2.
30. Macchi EG, Gallati M, Braschi G, et al. Dielectric properties of RF heated ex vivo porcine liver tissue at 480 kHz: Measurements and simulations. J Phys D Appl Phys 2014; 47:485401.
31. Hoffmann R, Rempp H, Erhard L, et al. Comparison of four microwave ablation devices: An experimental study in ex vivo bovine liver. Radiology 2013;268:89–97.
32. Wang Y, Sun Y, Feng L, et al. Internally cooled antenna for microwave ablation: Results in ex vivo and in vivo porcine livers. Eur J Radiol 2008;67:357–361.
33. Lee JM, Han JK, Kim S, et al. Hepatic bipolar radiofrequency ablation using perfused-cooled electrodes: A comparative study in the ex vivo bovine liver. Br J Radiol 2004;77:944–949.
34. Zu TN, Athamneh AI, Collakova E, et al. Assessment of ex vivo perfused liver health by Raman spectroscopy. J Raman Spectrosc 2015;46:551–558.
35. Bhonsle S, Bonakdar M, Neal RE, 2nd, et al. Characterization of irreversible electroporation ablation with a validated perfused organ model. J Vasc Interv Radiol 2016;27: 1913–1922.e1912. DOI: 10.1016/j.jvir.2016.07.012
36. Mikhail AS, Negussie AH, Graham C, et al. Evaluation of a tissue-mimicking thermochromic phantom for radiofrequency ablation. Med Phys 2016;43:4304–4311.
37. Michna R, Gadde M, Ozkan A, et al. Vascularized microfluidic platforms to mimic the tumor microenvironment. Biotechnol Bioeng 2018;115:2793–2806.
38. Saadi W, Wang S-J, Lin F, et al. A parallel-gradient microfluidic chamber for quantitative analysis of breast cancer cell chemotaxis. Biomed Microdevices 2006;8:109–118.
39. Sano MB, Fesmire CC, DeWitt MR, et al. Burst and continuous high frequency irreversible electroporation protocols evaluated in a 3D tumor model. Phys Med Biol 2018; 63:135022. DOI: 10.1088/1361–6560/aacb62
40. Arena CB, Szot CS, Garcia PA, et al. A three-dimensional in vitro tumor platform for modeling therapeutic irreversible electroporation. Biophys J 2012;103:2033–2042. DOI: 10.1016/j.bpj.2012.09.017
41. Negussie AH, Partanen A, Mikhail AS, et al. Thermochromic tissue-mimicking phantom for optimisation of thermal tumour ablation. Int J Hyperthermia 2016;32:239–243.
42. Eranki A, Mikhail AS, Negussie AH, et al. Tissue-mimicking thermochromic phantom for characterization of HIFU devices and applications. Int J Hyperthermia 2019;36:518–529.
43. Pearce J. Irreversible tissue thermal alterations: Skin burns, thermal damage and cell death. Theory Appl Heat Transf Hum 2018;2:553–590.
44. de Jong TL, Pluymen LH, van Gerwen DJ, et al. PVA matches human liver in needle-tissue interaction. J Mech Behav Biomed Mater 2017;69:223–228.
45. Geckil H, Xu F, Zhang X, et al. Engineering hydrogels as extracellular matrix mimics. Nanomedicine 2010;5:469–484.
46. Sano MB, Fan RE, Hwang GL, et al. Production of spherical ablations using nonthermal irreversible electroporation: A laboratory investigation using a single electrode and grounding pad. J Vasc Interv Radiol 2016;27: 1432–1440.e1433. DOI: 10.1016/j.jvir.2016.05.032
47. Kaufman JD, Fesmire CC, Petrella RA, et al. High-frequency irreversible electroporation using 5,000-V waveforms to create reproducible 2-and 4-cm ablation zones—A laboratory investigation using mechanically perfused liver. J Vasc Interv Radiol 2020;31:162–168.e7.
48. DeWitt MR, Latouche EL, Kaufman JD, et al. Simplified nonthermal tissue ablation with a single insertion device enabled by bipolar high-frequency pulses. IEEE Trans Biomed Eng 2020;67:2043–2051. DOI: 10.1109/TBME.2019.2954122
49. Sano MB, Petrella RA, Kaufman JA, et al. Electro-thermal therapy: Microsecond duration pulsed electric field tissue ablation with dynamic temperature control algorithms. Comput Biol Med 2020;121:103807.
50. Sano MB, Fesmire CC, Petrella RA. Electro-thermal therapy algorithms and active internal electrode cooling reduce thermal injury in high frequency pulsed electric field cancer therapies. Ann Biomed Eng 2020 [Epub ahead of print]; DOI: 10.1007/s10439-020-02524-x
51. Haemmerich D, Staelin ST, Tsai J-Z, et al. In vivo electrical conductivity of hepatic tumours. Physiol Meas 2003; 24:251.
52. Maor E, Ivorra A, Rubinsky B. Non thermal irreversible electroporation: Novel technology for vascular smooth muscle cells ablation. PLoS One 2009;4:e4757.
53. Daniels C, Rubinsky B. Electrical field and temperature model of nonthermal irreversible electroporation in heterogeneous tissues. J Biomech Eng 2009;131:071006.
54. Phillips M, Maor E, Rubinsky B. Nonthermal irreversible electroporation for tissue decellularization. J Biomech Eng 2010;132:091003. DOI: 10.1115/1.4001882
55. Fesmire CC, Petrella RA, Fogle CA, et al. Temperature dependence of high frequency irreversible electroporation evaluated in a 3D tumor model. Ann Biomed Eng 2020;48: 2233–2246.
56. Nuccitelli R. Application of pulsed electric fields to cancer therapy. Bioelectricity 2019;1:30–34.
57. Niessen C, Thumann S, Beyer L, et al. Percutaneous Irreversible Electroporation: Long-term survival analysis of 71 patients with inoperable malignant hepatic tumors. Sci Rep 2017;7:43687.
58. Lundy M, Garland-Kledzik M, Shen P. Arterio-enteric fistula after irreversible electroporation. Am Surg 2019;85: E55–E57.
59. Narayanan G, Bhatia S, Echenique A, et al. Vessel patency post irreversible electroporation. Cardiovasc Intervent Radiol 2014;37:1523–1529.
60. Sano MB, DeWitt MR, Teeter SD, et al. Optimization of a single insertion electrode array for the creation of clinically relevant ablations using high-frequency irreversible electroporation. Comput Biol Med 2018;95:107–117. DOI: 10.1016/j.compbiomed.2018.02.009

61. Kodama H, Vroomen LG, Ueshima E, et al. Catheter based endobronchial electroporation is feasible for the focal treatment of peri-bronchial tumors. J Thorac Cardiovasc Surg 2018;155:2150–2159.e3.
62. Van Gerwen D, Dankelman J, Van Den Dobbelsteen J. Measurement and stochastic modeling of kidney puncture forces. Ann Biomed Eng 2014;42:685–695.
63. Baharin RHM, Uno T, Arima T, et al. Effects of the permittivity and conductivity of human body for normal-mode helical antenna performance. IEICE Electron Expr 2019; 16:20190395.
64. Arena CB, Sano MB, Rylander MN, et al. Theoretical considerations of tissue electroporation with high-frequency bipolar pulses. IEEE Trans Biomed Eng 2011;58:1474–1482. DOI: 10.1109/TBME.2010.2102021
65. Bakker A, van der Zee J, van Tienhoven G, et al. Temperature and thermal dose during radiotherapy and hyperthermia for recurrent breast cancer are related to clinical outcome and thermal toxicity: A systematic review. Int J Hyperthermia 2019;36:1023–1038.
66. Yarmolenko PS, Moon EJ, Landon C, et al. Thresholds for thermal damage to normal tissues: An update. Int J Hyperthermia 2011;27:320–343.
67. Pearce JA. Relationship between Arrhenius models of thermal damage and the CEM 43 thermal dose. In: Energy-based Treatment of Tissue and Assessment V. Proceedings of the International Society for Optics and Photonics. San Jose, California, 2009: 718104.
68. Mouratidis PX, Rivens I, Civale J, et al. Relationship between thermal dose and cell death for ''rapid'' ablative and ''slow'' hyperthermic heating. Int J Hyperthermia 2019;36: 228–242.
69. Dewhirst MW, Viglianti B, Lora-Michiels M, et al. Basic principles of thermal dosimetry and thermal thresholds for tissue damage from hyperthermia. Int J Hyperthermia 2003; 19:267–294.
70. Petrella RA, Fesmire CC, Kaufman JA, et al. Algorithmically controlled electroporation: A technique for closed loop temperature regulated pulsed electric field cancer ablation. IEEE Trans Biomed Eng 2020;67:2176–2186.
71. Ivey JW, Latouche EL, Sano MB, et al. Targeted cellular ablation based on the morphology of malignant cells. Sci Rep 2015;5:17157. DOI: 10.1038/srep17157

Address correspondence to:
Michael B. Sano, PhD
UNC/NCSU Joint Department
of Biomedical Engineering
911 Oval Drive
Engineering Building 3
Raleigh, NC 27606
USA

Email: mikesano@med.unc.edu